CrossMark

Generation of He I 1083 nm Images from SDO AIA Images by Deep Learning

Jihyeon Son[1] , Junghun Cha[2] , Yong-Jae Moon[1,2] , Harim Lee[2] , Eunsu Park[2] , Gyungin Shin[3], and Hyun-Jin Jeong[1]

[1] School of Space Research, Kyung Hee University, Yongin, 17104, Republic Of Korea; moonyj@khu.ac.kr
[2] Department of Astronomy and Space Science, Kyung Hee University, Yongin, 17104, Republic Of Korea
[3] Department of Engineering Science, University of Oxford, Oxford, United Kingdom

Abstract

In this study, we generate He I 1083 nm images from Solar Dynamic Observatory (SDO)/Atmospheric Imaging Assembly (AIA) images using a novel deep learning method (pix2pixHD) based on conditional Generative Adversarial Networks (cGAN). He I 1083 nm images from National Solar Observatory (NSO)/Synoptic Optical Long-term Investigations of the Sun (SOLIS) are used as target data. We make three models: single-input SDO/ AIA 19.3 nm for Model I, single-input 30.4 nm image for Model II, and double-input (19.3 and 30.4 nm) images for Model III. We use data from 2010 October to 2015 July except for June and December for training and the remaining one for test. Major results of our study are as follows. First, the models successfully generate He I 1083 nm images with high correlations. Second, Model III shows better results than those with one input image in terms of metrics such as correlation coefficient (CC) and root mean square error (RMSE). CC and RMSE between real and synthetic ones for model III with 4 by 4 binnings are 0.88 and 9.49, respectively. Third, synthetic images show well observational features such as active regions, filaments, and coronal holes. This work is meaningful in that our model can produce He I 1083 nm images with higher cadence without data gaps, which would be useful for studying the time evolution of the chromosphere and transition region.

Unified Astronomy Thesaurus concepts: The Sun (1693); Solar chromosphere (1479); Convolutional neural networks (1938); Solar filaments (1495); Solar coronal holes (1484)

Supporting material: animation

1. Introduction

The He I 1083 nm line is a spectral line formed at the upper chromosphere and lower transition region in the Sun. He I 1083 nm spectroheliograms show both chromospheric and coronal structures such as coronal holes, filaments, and filament channels. Especially, they have been mainly used to observe coronal holes at ground. Coronal holes indicate regions where the solar corona is colder and has lower plasma densities compared to surroundings. They are well known as the source of high-speed solar wind owing to their open magnetic fields. Therefore, they have been regarded as an important component for forecasting space weather, and they have been observed in several wavelengths such as extreme-ultraviolet (EUV), X-ray, and infrared lines. Unlike EUV and X-ray observations, they appear bright in He I 1083 nm images. This is because coronal radiation overpopulates the He I 1083 multiplet transition levels, resulting in the increase of the absorption at places where the coronal radiation is high (Harvey & Recely 2002). In other words, the absorption of the He I 1083 nm line decreases in coronal holes where coronal radiation is low. Such characteristics in He I 1083 nm make it possible to indicate a more precise shape of coronal holes without disturbance of bright structures at the line of sight than in X-rays. Because of this advantage, He I 1083 nm images have been used for the study of coronal holes by several authors (Fox et al. 1998; Harvey & Recely 2002; Malanushenko & Jones 2005; Wang 2017; Wallace et al. 2019). Henney & Harvey (2005) developed a method for automated coronal hole detection with He I 1083 nm images and magnetograms. De Toma et al. (2005) observed transient coronal holes that form during the onset of coronal mass ejections (CMEs) using He I 1083 nm data. In addition, they are used for not only coronal holes but

also active regions and filaments (Harvey & Recely 1984; MacQueen et al. 2000; Yang et al. 2008; Kuckein et al. 2012; Wang et al. 2016; Baranovskii et al. 2017).

Deep learning is a branch of machine learning in which a computer forms an artificial neural network similar to a human's brain to solve complex nonlinear relationships. Deep learning has widely been used to handle multiple problems in various fields. In particular, image-to-image translation methods based on Generative Adversarial Networks (GANs; Goodfellow et al. 2014) have been successfully used. One of the most well-known methods among them is "pix2pix" (Isola et al. 2017) based on conditional GAN (cGAN; Mirza & Osindero 2014). There have been several researches in the astronomy field using it, and they show competent results (Kim et al. 2019; Park et al. 2019, 2020; Ji et al. 2020; Lee et al. 2021, 2021). However, the pix2pix has a drawback of poor results with artifacts and lack of details when performing high-resolution image generation. To solve this problem, Wang et al. (2018) proposed the "pix2pixHD" model with a novel adversarial loss and multiscale network architectures. Shin et al. (2020) successfully generated solar magnetograms with 1024×1024 pixel resolution from Ca II K images using the pix2pixHD. Jeong et al. (2020) developed a model based on the pix2pixHD to generate solar farside magnetograms from EUV images and then extrapolated the global magnetic fields using frontside and synthetic farside data. Their results show that the pix2pixHD method is appropriate for translating between high-resolution solar images having different wavelengths.

In this paper, we present three models to generate synthetic He I 1083 nm images from Solar Dynamic Observatory (SDO; Pesnell et al. 2011)/Atmospheric Imaging Assembly (AIA; Lemen et al. 2012) images using pix2pixHD. For this work, we use 19.3 and 30.4 nm images as input data and He I 1083 nm

images from Synoptic Optical Long-term Investigations of the Sun (SOLIS; Keller et al. 2003) as target data. This study has several advantages. First, we can generate He I 1083 nm images with high spatial resolution and uniform quality regardless of seeing conditions. Second, we can produce synthetic He I 1083 nm images with a high time cadence of 12 s. Third, we can fill up observational gaps caused by instrumental problems and/or nighttime. To the best of our knowledge, our study is the first trial to generate ground-based data by deep learning.

This paper is organized as follows. We introduce detailed explanations of our data and models in Sections 2 and 3, respectively. We evaluate our models with metrics and discuss the results in Section 4. Finally, we summarize and conclude our study in Section 5.

2. Data

AIA is one of the instruments of SDO that provides simultaneous high-resolution solar full-disk images of the corona and transition region in multiple wavelengths with 12 s temporal resolution (Lemen et al. 2012). Among the provided passband data, we choose 19.3 and 30.4 nm as input data of our model. The 19.3 nm data represent solar corona, and 30.4 nm data represent solar chromosphere, so that we can expect that the model can generate both coronal and chromospheric structures seen in He I 1083 nm observations. The SDO/AIA data are available from the Joint Science Operation Center (JSOC) database (http://jsoc.stanford.edu/ajax/lookdata.html).

SOLIS has three instruments, including Vector Spectro-magnetograph, which is a 50 cm effective aperture reflective telescope (Keller et al. 2003). VSM provides photospheric and chromospheric full-disk vector-magnetograms and He I 1083 nm line observations. We use daily full-disk images of equivalent width in He I 1083 nm for target data of our model. The observation of He I 1083 nm by this instrument ended in 2015 July.

For SDO/AIA data, we use better-quality images with the quality index of zero in the header information. We make level 1.5 images using the *aiaprep* library from the Sunpy (The SunPy Community et al. 2020) software package, which processes rotating, centering, and aligning axis. To make images have the same exposure condition, we divide the data number by exposure time. We use the data that are scaled from 0 to 2^{12} DN s^{-1}. We choose this range by referring to count rates in Boerner et al. (2012). Then, we divide them by median values on the solar disk to calibrate the data (Ugarte-Urra et al. 2015; Jeong et al. 2020) and take the logarithm of them. In the case of He I 1083 nm data, we use geometry-corrected level 2 data. The data are available from the SOLIS homepage (https://solis.nso.edu/0/vsm/VSMDataSumm.php). We adopt the data that are scaled from −150 to 100, which is a typical approach (https://solis.nso.edu). Note that limb darkening was not compensated very well on the He I 1083 nm data we used, thus hiding polar coronal holes. This is due to equivalent width processing for observations by SOLIS. A detailed data description is given at the SOLIS website.[4] For He I 1083 nm images, we check all images by visual inspection and remove improper data having noisy and

missing information. Original pixel sizes of SDO/AIA and He I 1083 nm data are 4096 × 4096 and 2048 × 2048, respectively. For training, they are resized to 1024 × 1024 pixels.

The total period of data used in this study is from 2010 October to 2015 July. After the preprocessing described above, we get a total of 1123 pairs of images. The data except June and December (915 pairs) are used for training, and the remaining ones (208 pairs) for test. This is because we want to take into account the solar cycle effect in training and test.

3. Method

We use the "pix2pixHD" model, which is well known as an effective deep learning method for high-resolution image-to-image translation (Wang et al. 2018). The pix2pixHD consists of two main networks named "generator" and "discriminator." The training process of the pix2pixHD is as follows. At first, the generator produces target-like images from input images. The discriminator gets two pairs, a synthetic pair with synthetic and input images, and a real pair with target and input images. Then, the discriminator trains for distinguishing between the real pair and synthetic pair. The generator refers to this result and tries to generate more real-like images to deceive the discriminator.

In the generator, several convolution layers and transposed convolution layers are stacked. A convolution layer has major parameters named kernels (or filters) that extract features of input images. A transposed layer is an inverse of the convolution layer and generates an output image from extracted features. The discriminator consists of a number of convolution layers to classify real pairs and synthetic pairs. The kernels of convolution layers and transposed convolution layers are updated as training progresses. Our model has one generator and two discriminators (discriminator A and B) as shown in Figure 1. The two discriminators have the same network structure but work at different image scales. Discriminator A trains with original size images, and discriminator B trains with those downsampled by half. The multiscale discriminators help the generator to produce globally consistent images and finer details.

The pix2pixHD has two loss functions, Least Squares GAN (LSGAN; Mao et al. 2017) loss ($\mathcal{L}_{\mathrm{LSGAN}}$) and a feature matching loss ($\mathcal{L}_{\mathrm{FM}}$), to optimize the model. The LSGAN losses to update the generator and discriminator are given by

$$\mathcal{L}_{\mathrm{LSGAN}}^{G}(G, D) = (D(x, G(x)) - 1)^2$$
$$\mathcal{L}_{\mathrm{LSGAN}}^{D}(G, D) = \frac{1}{2}(D(x, y) - 1)^2 + \frac{1}{2}(D(x, G(x)))^2, \quad (1)$$

where x, y, and $G(x)$ are an input, a real output, and an output from the generator, respectively. The objective of the $\mathcal{L}_{\mathrm{FM}}$ is to match the distribution of the generated pair and real pair from multiple layers of the discriminator. The $\mathcal{L}_{\mathrm{FM}}$ is obtained by

$$\mathcal{L}_{\mathrm{FM}}(G, D) = \sum_{i=1}^{T} \frac{1}{N_i} [||D^{(i)}(x, y) - D^{(i)}(x, G(x))||_1], \quad (2)$$

where T, i, and N_i denote the total number of layers, the serial number of the layers, and the number of elements in each layer, respectively. We use a relative weight (λ) that controls the importance of $\mathcal{L}_{\mathrm{LSGAN}}^{G}$ and $\mathcal{L}_{\mathrm{FM}}$ (Wang et al. 2018). For our

---

[4] https://nispdata.nso.edu/webProdDesc2/presenter.php?file=solis_vsm_10830_sky_images.html&echoExact=0&name=SOLIS%20VSM%2010830%20full-disk%20images

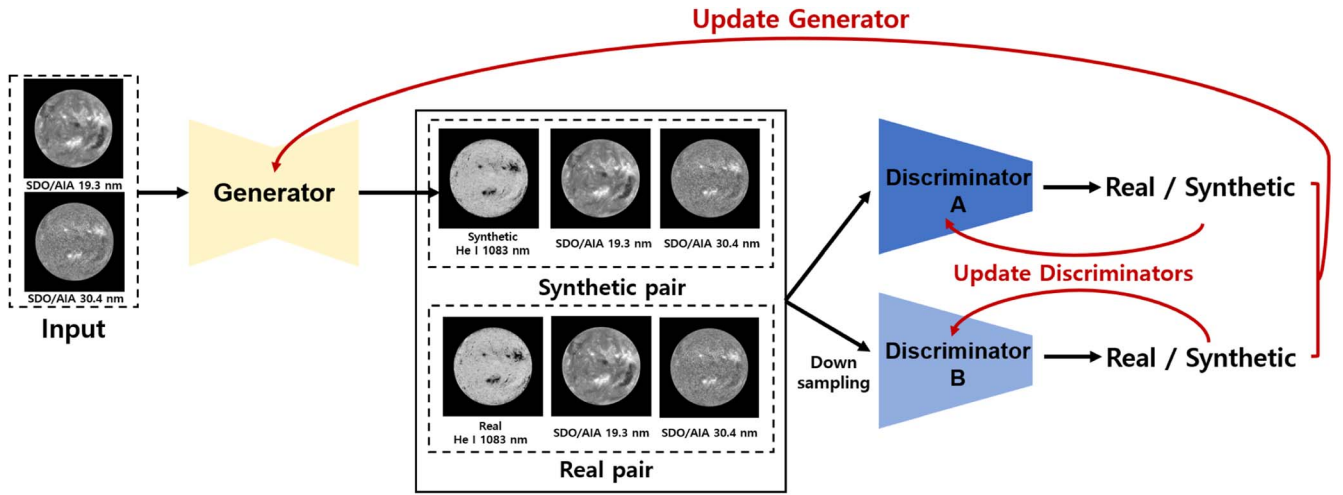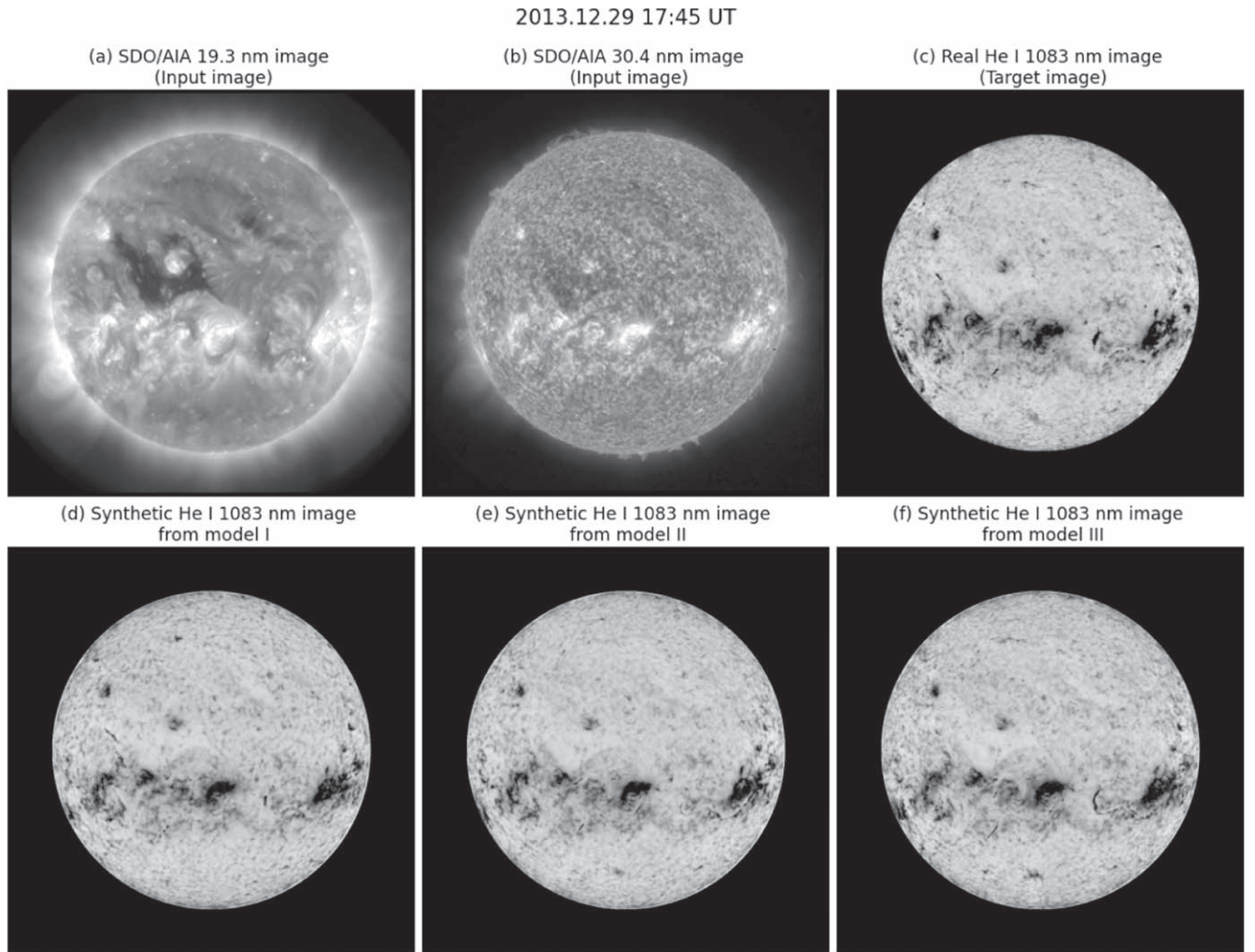**Figure 1.** Architecture of the model with two input images (model III).

Figure 2. Two input images, one target image and three synthetic from our three models at 17:45 UT on 2013 December 29. (a) SDO/AIA 19.3 nm image as input. (b) SDO/AIA 30.4 nm image as input. (c) He I 1083 nm image as target. (d) synthetic He I 1083 nm image from Model I. (e) Synthetic He I 1083 nm image from Model II. (f) Synthetic He I 1083 nm image from Model III.
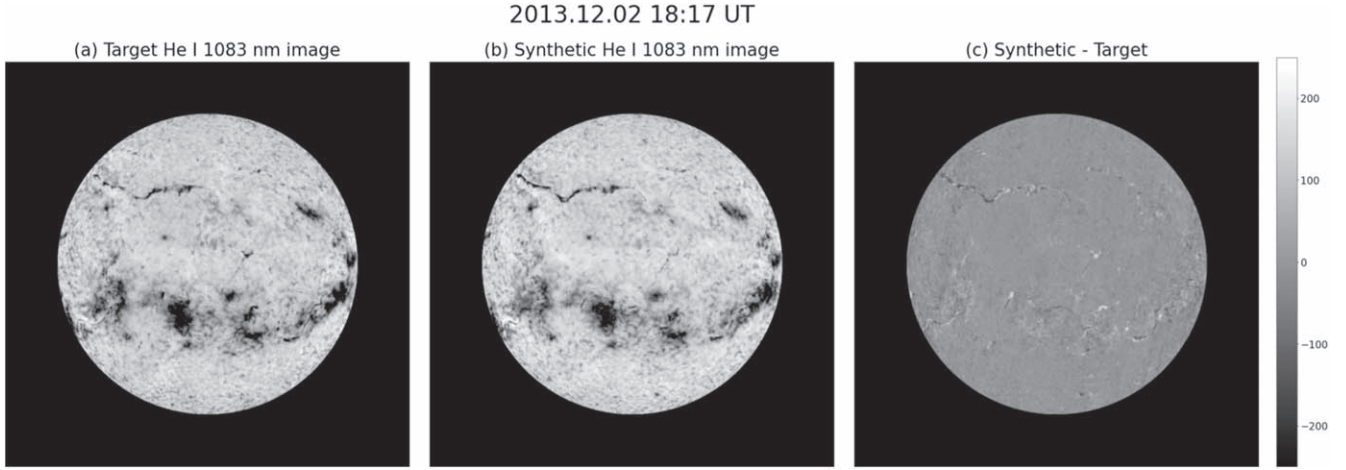
2013.12.02 18:17 UT

Figure 3. Comparison between the target He I 1083 nm image and synthetic one from Model III at 18:17 UT on 2013 December 2. (a) Target He I 1083 nm image; (b) synthetic He I 1083 nm image; (c) the difference map between panels (a) and (b).

model, we use 10 for λ as Wang et al. (2018) did. When the model is trained, the generator and discriminators try to minimize the losses given by

$$\min_G \left(\sum_{k=1,2} \mathcal{L}^G_{\text{LSGAN}}(G, D_k) + \lambda \sum_{k=1,2} \mathcal{L}_{\text{FM}}(G, D_k) \right)$$
$$\min_{D_1, D_2} \sum_{k=1,2} \mathcal{L}^D_{\text{LSGAN}}(G, D_k). \qquad (3)$$

To optimize the loss functions, we use the adaptive moment estimation (Adam; Kingma & Ba 2014) optimizer with learning late 0.0002.

In this study we make three models: a model with 19.3 nm images as input data (model I), a model with 30.4 nm images as input data (model II), and a model with both 19.3 and 30.4 nm images as input data (model III). These three models have the same architecture as shown in Figure 1. We train these models for 180,000 iterations (about 200 epochs). For evaluation, we save each model and synthetic image at every 5000th iterations. We evaluate all the saved models by metrics, and the results shown in the next section are the highest scores among them.

4. Results and Discussion

Figure 2 shows two input images, a target image and three synthetic images from our models (Model I, II, and III) at 17:45 UT on 2013 December 29. The overall distributions of the target image are well reproduced in the synthetic images, but there are a few differences in details between them. For Model I, it generates coronal holes clearly but cannot catch detailed structures such as filaments. On the other hand, for Model II, coronal holes in the generated images seem to be less precise than those from Model I. However, this model can capture the features that Model I misses. Because both 30.4 nm and He I 1083 nm are emitted from similar regions (chromosphere and transition region), it would be easier for Model II to find the relation between the two lines. Also, 30.4 nm images could have a small contribution from nearby coronal emission. Complementing each other's shortcomings, Model III with two input images generates He I 1083 nm images most plausibly.

Figure 3 shows a comparison between the target He I 1083 nm image and synthetic one from Model III at 18:17 UT on 2013 December 2. We make the difference map after

masking outside 0.95 $R_\odot$. We find that most values of the difference map are near zero as shown in Figure 3(c). Especially, there is little difference in coronal hole regions. On the other hand, there is a slight difference in the filament. This may be because the absorption process in filaments differs depending on wavelength. Dark features of extreme-ultraviolet (input wavelengths) can be explained by hydrogen Lyman continuum absorption (Schmahl & Orrall 1979). It is known that a high recombination rate from He$^+$ produces the absorption features at He I 1083 nm (Andretta & Jones 1997). The above absorption mechanisms make filaments appear differently in the corresponding images. To reduce the difference, more data sets for training and test may be needed. Nevertheless, the shape, location, and size of the filament in the two images are almost the same. Overall, it can be said that the model successfully generates the target-like images.

To evaluate our models quantitatively, we calculate the pixel-to-pixel Pearson correlation coefficient (CC) and root mean square error (RMSE) of each model for the test set. The closer CC is to 1, the higher linear relationship between two data. RMSE shows the differences between pixel values of real images and synthetic ones. CC and RMSE are given by

$$\text{CC} = \frac{\sum_{i=1}^N (X_i - \bar{X})(Y_i - \bar{Y})}{\sqrt{\sum_{i=1}^N (X_i - \bar{X})^2} \sqrt{\sum_{i=1}^N (Y_i - \bar{Y})^2}} \qquad (4)$$

$$\text{RMSE} = \sqrt{\frac{\sum_{i=1}^N (X_i - Y_i)^2}{N}}, \qquad (5)$$

where X, Y, $\bar{X}$, $\bar{Y}$, and N denote pixel values of generated images and real images, their average values, and total number of pixels, respectively. We obtain these metrics after performing 4×4 binning of images yielding 256×256 pixel size images, and we consider pixel values only inside 0.95 $R_\odot$ because of limb uncertainty. Table 1 shows the average of metrics of all our test data. As seen in Table 1, Model III shows the best performance in terms of both CC and RMSE values. This result coincides with the discussion of Figure 2. All results shown hereafter are generated by Model III.

To examine how well each of the specific structures is reproduced, we present pixel-by-pixel scatter plots between real and synthetic He I 1083 nm images for 182 filaments, 511 active
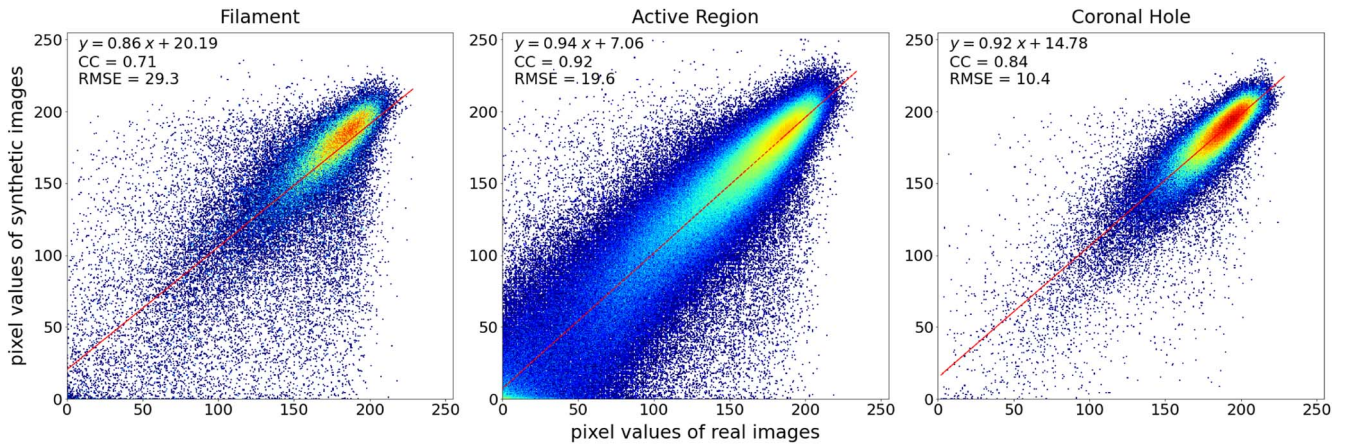
Figure 4. Pixel-by-pixel scatter plots between real and synthetic He I 1083 nm images for 182 filaments, 511 active regions, and 74 coronal holes (left to right).

Table 1
The Average Pixel-to-pixel Correlation Coefficient (CC) and Root Mean Square Error (RMSE) after 4×4 Binning between Real He I 1083 Images and Synthetic Ones from Our Models

	Model I (input: 19.3 nm)	Model II (input: 30.4 nm)	Model III (input: 19.3 and 30.4 nm)
Mean pixel-to-pixel CC (4×4 binning)	0.83	0.86	**0.88**
Mean RMSE (4×4 binning)	11.28	10.15	**9.49**

regions, and 74 coronal holes in Figure 4. The scatter plots are made after 4×4 binning. These events are all significantly large in view of space weather forecasting. For this, we crop each feature using coordinate information from Heliophysics Events Knowledgebase (HEK) provided by Lockheed Martin Solar and Astrophysics Laboratory (LMSAL). For evaluation we obtain CC and RMSE for each structure as we did for the full-disk data, and they are shown in each scatter plot. Three features have good CC and RMSE values, which are similar to those of the full-disk data. Especially, active regions and coronal holes show better results than filaments. This is in the same line with the discussion of the above difference map (Figure 3).

To demonstrate that our model can generate coronal holes well, we try to detect coronal holes from the target and synthetic images and then compare them. For this, we refer to the recipe of automatic coronal hole detection in Henney & Harvey (2005). A key point of their process is using pixel values to find the boundaries of coronal holes. This takes advantage that coronal holes seem brighter than the surroundings in He I 1083 nm images. A more detailed procedure is described in Henney & Harvey (2005). We apply the same method to the target image and synthetic image at 17:45 UT on 2013 December 29, and the results are shown in Figure 5. As shown in Figures 5(a) and (c), the locations of coronal holes in the synthetic image are almost identical to those of the real one. Also, there are no noticeable differences in the overall forms as seen in Figures 5(b) and (d). These results show that our model can well reproduce coronal holes. It is more reliable to combine various wavelengths than when using only one passband for determining boundaries of coronal holes because their forms

depend on observation wavelength (Toma & Arge 2005). We expect that using synthetic images from our model with the observation data in different wavelengths is helpful for studying coronal holes in this respect. In addition, to check the coronal hole identification near the limb, we divide the coronal holes used in Figure 4 into two groups: (A) within $60°$, and (B) the others. The A group has 48 coronal holes, and the B group has 26. We calculate CC and RMSE of each group. The A group shows 0.83 and 10.1 for CC and RMSE, respectively, and the B group shows 0.85 and 11.0, respectively. This result shows that our model generates coronal holes without significant differences depending on location.

Figure 6(c) shows an abnormal He I 1083 nm observation because of the malfunction of the instrument on 2012 August 23. In the image, active regions and coronal holes cannot be identified. Using SDO/AIA data at the same time, we can generate the He I 1083 nm image using Model III in Figure 6(d). Comparing SDO/AIA images (Figures 6(a) and (b)), the coronal holes and active regions that are invisible in Figure 6(c) are well reproduced in Figure 6(d). In addition, the seeing condition is not constant because He I 1083 nm data are observed at the ground. Therefore, the quality of the observations is nonuniform. However, our model can produce He I 1083 nm images with homogeneous data quality regardless of weather conditions. Also, our model can produce He I 1083 nm images at nighttime only if SDO/AIA data are available. These facts indicate that our model can be a method to overcome the limitations of ground-based observations.

We can fill in the data gap of He I 1083 nm observations by our model. For this we consider 2011 June, during when there are only 13 days of observations. Figure 7 shows daily He I 1083 nm images in 2011 June combining real observations and synthetic images. We generate daily He I 1083 nm data at 18:00 UT to complement the absences of observations. As a result, long-term synoptic evolution seen in the He I 1083 nm line can be shown without data gap. By synthetic images, we can identify the evolution of structures such as filaments, coronal holes, and active regions that are missed in real observations. Especially, we mark the evolution of a filament and coronal holes by yellow arrows and red arrows, respectively. Combining synthetic images and real observations makes it possible to continuously
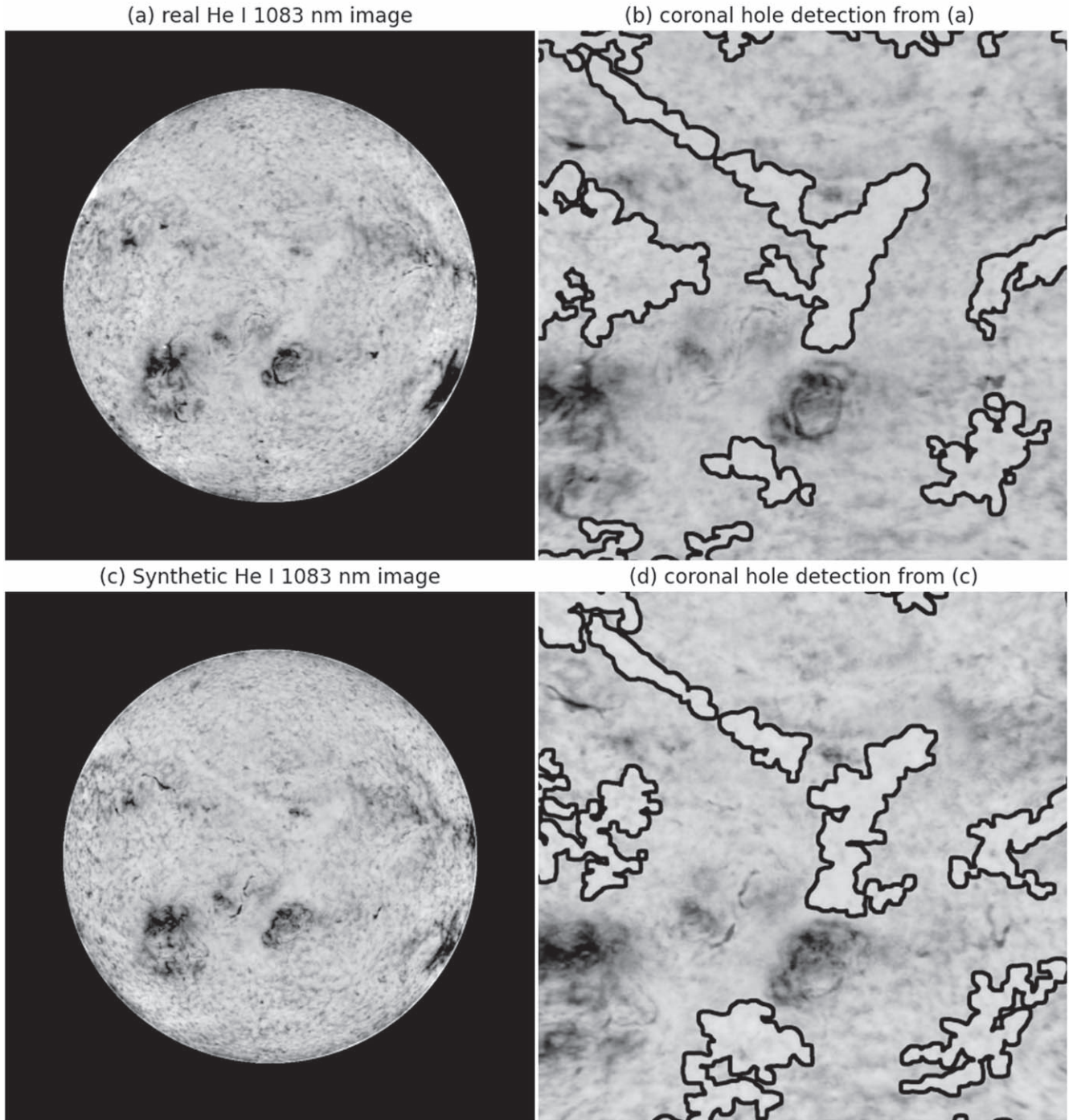
Figure 5. Coronal hole detection using the He I 1083 nm image at 16:41 UT on 2013 June 26. Panels (a) and (c) show real and synthetic He I 1083 nm images, respectively. Panels (b) and (d) are zoomed-in images of the coronal hole region in panels (a) and (c), respectively.

monitor temporal evolution of structures in the chromosphere and transition region.

Filaments are one of the important chromospheric features because their eruptions are known to be associated with CMEs. However, the entire filament eruption process cannot be monitored in He I 1083 nm observations owing to their low cadence and/or seeing conditions and/or instrumental problems. Because filaments clearly appear in He I 1083 nm data, it is very useful to study the evolution of filaments if we can observe them continuously. Figure 8 shows synthetic He I 1083 nm images during filament

eruption from 21:10 UT on 2016 February 18 to 00:20 UT on February 19. The model generates the images every 10 minutes. The process of filament eruption is well shown in Figure 8. This result suggests a sufficient possibility to study the eruption of filaments with a high time cadence.

5. Conclusion

In this study, we have developed three deep learning models to generate synthetic He I 1083 nm images from SDO/AIA
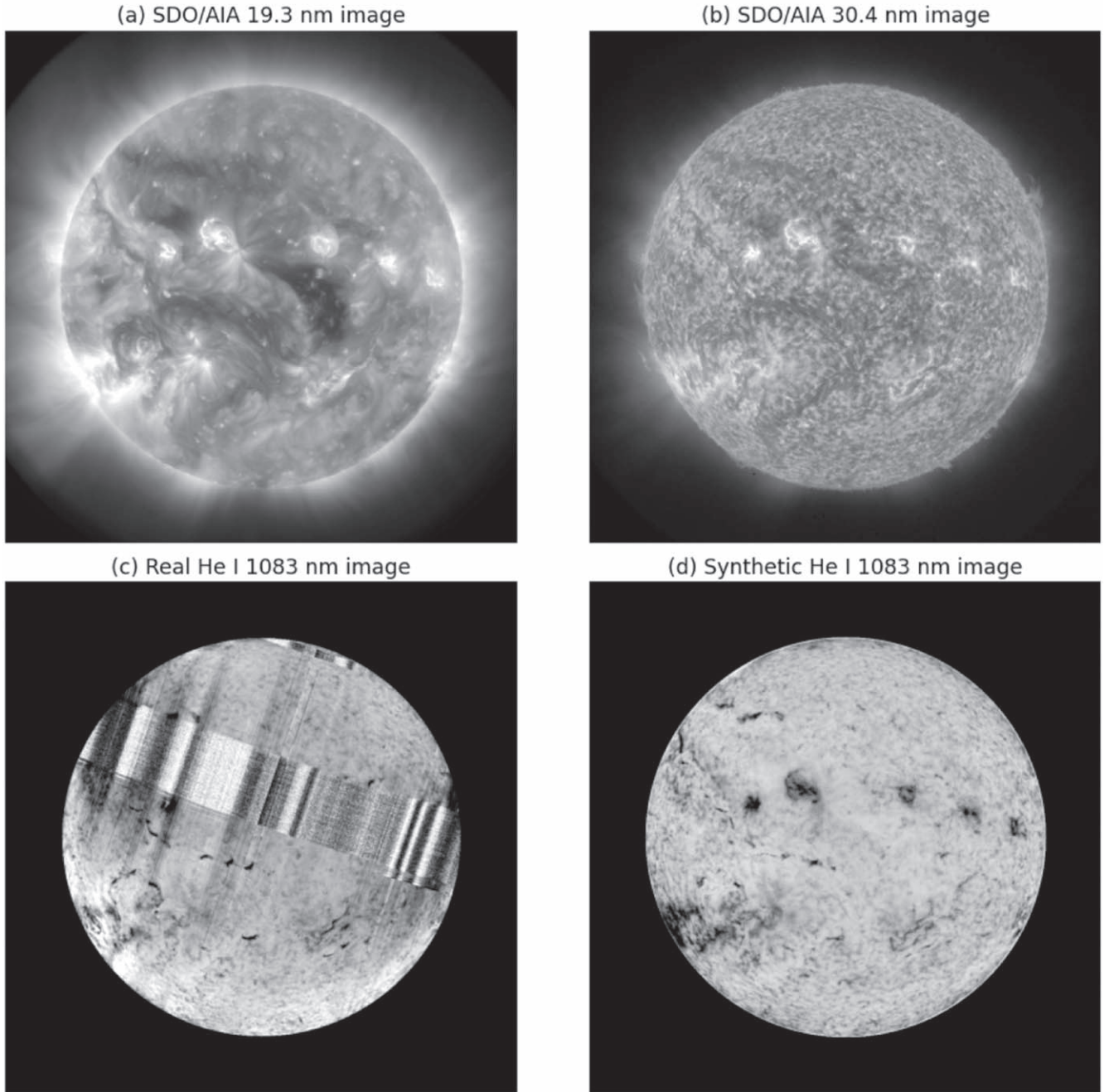
2012.08.23 22:08 UT

(a) SDO/AIA 19.3 nm image

(b) SDO/AIA 30.4 nm image

(c) Real He I 1083 nm image

(d) Synthetic He I 1083 nm image

Figure 6. Restoration of damaged He I 1083 nm data at 22:08 UT on 2012 August 23 by our model. (a) SDO/AIA 19.3 nm image as input; (b) SDO/AIA 30.4 nm image as input; (c) real He I 1083 nm image; (d) synthetic image from Model III.

images. To treat high-resolution (1024 × 1024 pixels) images, we apply the pix2pixHD model to these data. We train the following models: single-input SDO/AIA 19.3 nm image for Model I, single-input 30.4 nm image for Model II, and double-input (19.3 and 30.4 nm) images for Model III. Target data of all the models are He I 1083 nm images from NSO/SOLIS. The summaries of this study are as follows. First, the models successfully generate He I 1083 nm images from SDO/AIA images. Especially, Model III shows the best performance in terms of metrics and visual aspects. Second, pixel-to-pixel CC

and RMSE values after 4 × 4 binning of Model III are 0.88 and 9.49, respectively. Third, the boundaries of coronal holes from the synthetic images are well consistent with those from real ones. Fourth, the synthetic He I 1083 nm images are generated with uniform quality and high time resolution regardless of instrumental problems and atmospheric conditions. This implies that our model should be a reliable tool for studying the time evolution of chromospheric phenomena. Our study may be extended to modernize He I 1083 nm data whose observations began 45 yr ago. Recently, Pineci et al. (2021)
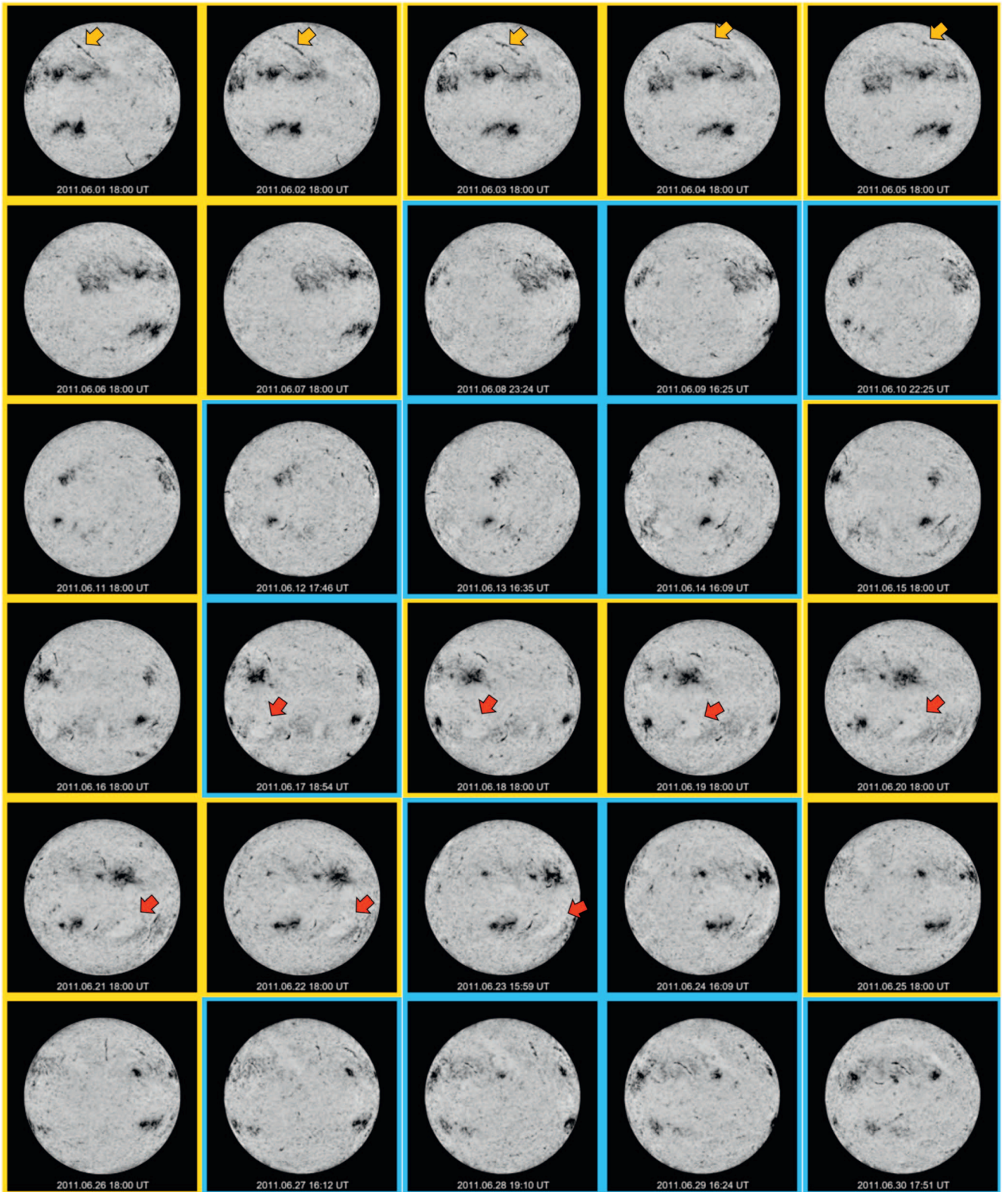
Figure 7. Filling in the absence of He I 1083 nm observations by our model in 2011 June. The blue boxes are real He I 1083 nm observations, and the yellow boxes are synthetic images when the observations are absent. The yellow arrows follow the evolution of a filament, and the red arrows indicate the evolution of coronal holes.

generated 30.4 nm images from He I 1083 nm images by deep learning. If historical 30.4 nm images are generated by their model, our model together with their results may be used for modernizing the He I 1083 nm images. We leave this to a future work. Our results show a possibility that the deep learning method could help overcome shortcomings of various ground-based observations.
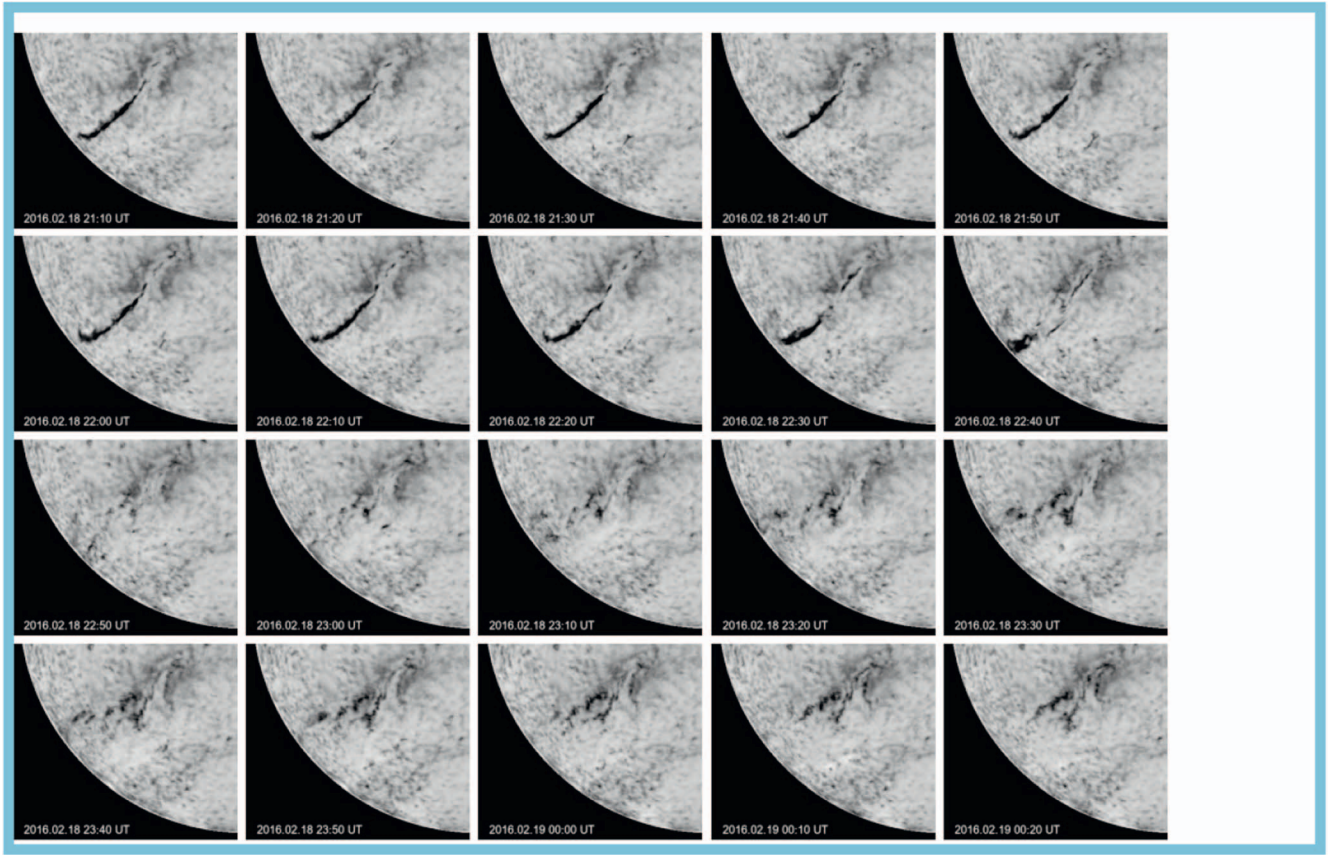
Figure 8. Synthetic He I 1083 nm images during filament eruption from 21:10 UT on 2016 February 18 to 00:20 UT on February 19. They are generated every 10 minutes. An animation of this figure with 1-minute cadence is available. The animation starts at 2016 February 18 at 21:10 UT and ends the next day at 00:29 UT. (An animation of this figure is available.)

ORCID iDs

Jihyeon Son ● https://orcid.org/0000-0003-2678-5718
Yong-Jae Moon ● https://orcid.org/0000-0001-6216-6944
Harim Lee ● https://orcid.org/0000-0002-9300-8073
Eunsu Park ● https://orcid.org/0000-0003-0969-286X

Hyun-Jin Jeong ● https://orcid.org/0000-0003-4616-947X

References

Andretta, V., & Jones, H. P. 1997, ApJ, 489, 375
Baranovskii, E., Stepanyan, N., Tarashchuk, V., & Shtertser, N. 2017, ARep, 61, 74
Boerner, P., Edwards, C., Lemen, J., et al. 2012, SoPh, 275, 41
De Toma, G., Holzer, T., Burkepile, J., & Gilbert, H. 2005, ApJ, 621, 1109
Fox, P., McIntosh, P., & Wilson, P. 1998, SoPh, 177, 375
Goodfellow, I., Pouget-Abadie, J., Mirza, M., et al. 2014, in Advances in Neural Information Processing Systems 27, ed. Z. Ghahramani et al. (Red Hook, NY: Curran Associates, Inc.), 2672
Harvey, K. L., & Recely, F. 1984, SoPh, 91, 127
Harvey, K. L., & Recely, F. 2002, SoPh, 211, 31
Henney, C. J., & Harvey, J. W. 2005, in ASP Conf. Ser., 346, Large-scale Structures and their Role in Solar Activity, ed. K. Sankarasubramanian, M. Penn, & A. Pevtsov (San Francisco, CA: ASP), 261
Isola, P., Zhu, J.-Y., Zhou, T., & Efros, A. A. 2017, in Proc. IEEE Conf. on Computer Vision and Pattern Recognition (Los Alamitos, CA: IEEE Computer Society), 5967
Jeong, H.-J., Moon, Y.-J., Park, E., & Lee, H. 2020, ApJL, 903, L25
Ji, E.-Y., Moon, Y.-J., & Park, E. 2020, SpWea, 18, e2019SW002411
Keller, C. U., Harvey, J. W., & Giampapa, M. S. 2003, Proc. SPIE, 4853, 194
Kim, T., Park, E., Lee, H., et al. 2019, NatAs, 3, 397
Kingma, D. P., & Ba, J. 2014, arXiv:1412.6980
Kuckein, C., Martínez Pillet, V., & Centeno, R. 2012, A&A, 539, A131
Lee, H., Park, E., & Moon, Y.-J. 2021, ApJ, 907, 118
Lee, S., Ji, E.-Y., Moon, Y.-J., & Park, E. 2021, SpWea, 19, e2600
Lemen, J. R., Title, A. M., Akin, D. J., et al. 2012, SoPh, 275, 17
MacQueen, R., Hendrickson, M., Woods, J., et al. 2000, SoPh, 191, 85
Malanushenko, O. V., & Jones, H. P. 2005, SoPh, 226, 3

Mao, X., Li, Q., Xie, H., et al. 2017, in Proc. IEEE Int. Conf. on Computer Vision (Los Alamitos, CA: IEEE Computer Society), 2813

Mirza, M., & Osindero, S. 2014, CoRR, arXiv:1411.1784

Park, E., Moon, Y.-J., Lee, J.-Y., et al. 2019, ApJL, 884, L23

Park, E., Moon, Y.-J., Lim, D., & Lee, H. 2020, ApJL, 891, L4

Pesnell, W. D., Thompson, B. J., & Chamberlin, P. 2011, The Solar Dynamics Observatory (Berlin: Springer), 3

Pineci, A., Sadowski, P., Gaidos, E., & Sun, X. 2021, ApJL, 910, L25

Schmahl, E. J., & Orrall, F. Q. 1979, ApJL, 231, L41

Shin, G., Moon, Y.-J., Park, E., et al. 2020, ApJL, 895, L16

The SunPy Community, Barnes, W. T., Bobra, M. G., et al. 2020, ApJ, 890, 68

Toma, G. D., & Arge, C. N. 2005, in ASP Conf. Ser., 346, Large-scale Structures and their Role in Solar Activity, ed. K. Sankarasubramanian, M. Penn, & A. Pevtsov (San Francisco, CA: ASP), 251

Ugarte-Urra, I., Upton, L., Warren, H. P., & Hathaway, D. H. 2015, ApJ, 815, 90

Wallace, S., Arge, C., Pattichis, M., Hock-Mysliwiec, R., & Henney, C. 2019, SoPh, 294, 19

Wang, T.-C., Liu, M.-Y., Zhu, J.-Y., et al. 2018, in Proc. IEEE Conf. on Computer Vision and Pattern Recognition (Los Alamitos, CA: IEEE Computer Society), 8798

Wang, Y., Su, Y., Hong, Z., et al. 2016, ApJ, 833, 250

Wang, Y. M. 2017, ApJ, 841, 94

Yang, L.-H., Jiang, Y.-C., & Ren, D.-B. 2008, ChJAA, 8, 329